Inorganic Chemistry
Article
pubs.acs.org/IC

Structures and Magnetism of the Rare-Earth Orthochromite Perovskite Solid Solution $La_xSm_{1-x}CrO_3$

Luke M. Daniels,[†] Mads. C. Weber,[‡,⊥] Martin R. Lees,[§] Mael Guennou,[‡] Reza J. Kashtiban,[§] Jeremy Sloan,[§] Jens Kreisel,[‡] and Richard I. Walton*[,†]

[†]Department of Chemistry and [§]Department of Physics, University of Warwick, Coventry, CV4 7AL, U.K.
[‡]Département Sciences et Analyses des Matériaux, CRP Gabriel Lippmann, 41, Rue du Brill, 4422 Belvaux, Luxembourg
[⊥]University of Luxembourg, 1511 Luxembourg, Luxembourg

Supporting Information

ABSTRACT: A new mixed rare-earth orthochromite series, $La_xSm_{1-x}CrO_3$, prepared through single-step hydrothermal synthesis is reported. Solid solutions (x = 0, 0.25, 0.5, 0.625, 0.75, 0.875, and 1.0) were prepared by the hydrothermal treatment of amorphous mixed-metal hydroxides at 370 °C for 48 h. Transmission electron microscopy (TEM) reveals the formation of highly crystalline particles with dendritic-like morphologies. Rietveld refinements against high-resolution powder X-ray diffraction (PXRD) data show that the distorted perovskite structures are described by the orthorhombic space group *Pnma* over the full composition range. Unit cell volumes and Cr−O−Cr bond angles decrease monotonically with increasing samarium content, consistent with the presence of the smaller lanthanide in the structure. Raman spectroscopy confirms the formation of solid solutions, the degree of their structural distortion. With the aid of shell-model calculations the complex mixing of Raman modes below 250 cm^{-1} is clarified. Magnetometry as a function of temperature reveals the onset of low-temperature antiferromagnetic ordering of Cr^{3+} spins with weak ferromagnetic component at Néel temperatures (T_N) that scale linearly with unit cell volume and structural distortion. Coupling effects between Cr^{3+} and Sm^{3+} ions are examined with enhanced susceptibilities below T_N due to polarization of Sm^{3+} moments. At low temperatures the Cr^{3+} sublattice is shown to undergo a second-order spin reorientation observed as a rapid decrease of susceptibility.

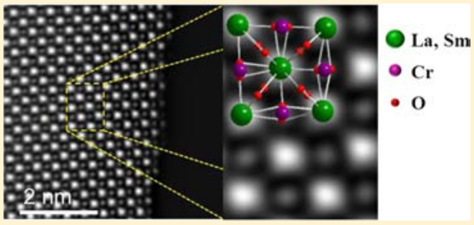

INTRODUCTION

The synthesis of rare-earth (R) transition metal (M) orthorhombic perovskite materials RMO_3 such as orthochromites $RCrO_3$, orthoferrites $RFeO_3$, and orthomanganites $RMnO_3$ has received great interest.[1] The perovskite structure is renowned for its structural versatility because of the wide selection of elements it can incorporate, driving structural distortions that influence, for example, magnetic and electronic properties and the interplay between the two.[2] The structure can also accommodate various types of disorder such as point substitutions or vacancies where in some cases, multiple A-site cations are needed to control and tune useful properties.[3] The rare-earth orthochromites with the orthorhombic *Pnma* structure display a multitude of different properties ranging from p-type semiconductor behavior,[4] catalytic activity toward the decomposition of N_2O gas into N_2 and O_2,[5] and doping alkali-earth metals into the structure gives rise to properties ideal for solid oxide fuel cell interconnect materials as well as for the oxidation of hydrocarbons.[6−9] Perhaps of most interest is the potential for magnetoelectric coupling that has led to further functionality beyond the electric and magnetic properties of the material.[10] Theoretical predictions of magnetoelectric coupling based on symmetry analysis revealed that an electric polarization, either spontaneous or induced by a magnetic field, can exist in the antiferromagnetically ordered phase.[11] Experimental observations of ferroelectricity and canted antiferromagnetism in several $RCrO_3$ and $YCrO_3$ support these results.[12−14] It was proposed that the electric polar ordering induced at the Cr^{3+} Néel temperature is due to interactions between the magnetic R^{3+} ions and the weakly ferromagnetically ordered Cr^{3+} sublattice.[14]

Owing to this plethora of useful properties, a variety of methods have been reported for the synthesis of $RCrO_3$ and their doped counterparts. These include traditional[15] and microwave-assisted[16] solid-state, solid-state metathesis of metal chloride salts,[17] self-propagating high temperature,[18] the calcination of coprecipitated precursors and sol−gel prepared citrates,[19,20] the hydrazine method,[21] and spray pyrolysis.[22] For all of these methods post-treatment annealing is usually necessary to achieve highly crystalline products, therefore introducing multiple steps into the synthesis.

One-step preparative methods such as solvothermal synthesis allow for soft chemical approaches to complex, multielement materials while providing some control over the product homogeneity, stoichiometry, and particle morphology.[23] Recently some of us reported a one-step hydrothermal synthesis for an entire range of $RCrO_3$.[24] Earlier attempts at

Received: August 6, 2013
Published: October 8, 2013

dx.doi.org/10.1021/ic402029u | *Inorg. Chem.* 2013, 52, 12161−12169

the hydrothermal synthesis of RCrO$_3$ materials focused solely on LaCrO$_3$,[25,26] where it was reported that successful crystallization could occur at temperatures as low as 260 °C, only if high KOH concentrations were used in week-long reactions.[27]

In contrast to the well-documented study of binary rare-earth chromites, the synthesis (by any route) of solid solutions containing multiple rare-earths are scarce; lanthanum materials, $La_{1-x}R_xCrO_3$ (where R = Pr, Nd, and Gd, and $x = 0.0 \le x \le 1.0$), have been prepared through traditional solid state techniques.[28−30] The properties of the materials were studied, but detailed structural analysis showing how a smaller lanthanide ion distorts the structure of LaCrO$_3$ is available only for $La_{1-x}Nd_xCrO_3$ ($0.0 \le x \le 1.0$).[31,32]

In this paper we present a one-step hydrothermal synthesis of a new series of materials $La_xSm_{1-x}CrO_3$ (x = 0, 0.25, 0.5, 0.625, 0.75, 0.875, and 1.0). We describe the results of detailed structural investigations from high-resolution diffraction and Raman spectroscopy that reveal the evolution of the distorted perovskite structure with samarium substitution, and discuss the effects this has on the magnetic properties. Systematic substitution of nonmagnetic La^{3+} for magnetic Sm^{3+} allows for the evolution of structural and magnetic properties to be studied, and coupling behavior between the magnetic Sm^{3+} (4f^5 shell electrons) and the existing weakly ferromagnetic Cr^{3+} (3d^3) sublattice to be observed.

■ EXPERIMENTAL METHODS

The hydrothermal synthesis of $La_xSm_{1-x}CrO_3$ was performed from amorphous mixed-metal hydroxide precursors, produced from hydrated rare-earth and chromium nitrates. To give solid solutions of desired compositions appropriate amounts of lanthanum(III) nitrate hexahydrate (99.999% Aldrich), samarium(III) nitrate hexahydrate (99.9% Aldrich), and chromium(III) nitrate nonahydrate (99% Aldrich) were dissolved into deionized water before adding 2 M KOH solution, resulting in the precipitation of a mixed-metal hydroxide gel. The gel was stirred for 15 min to ensure adequate mixing, before being separated from solution by suction filtration and washed profusely with deionized water to reduce the pH to neutral. Moisture was removed by drying for 3 days at 75 °C, before the green precipitate was ground into a fine powder. A hydrothermal multiautoclave system with 30 mL internal volume Inconnel vessels reported previously[24] was used to perform the hydrothermal treatment on the amorphous precursor. In this setup, the temperature and pressure within the vessels are digitally monitored throughout reactions. In a typical synthesis ∼350 mg of the dried amorphous precursor was placed inside an Inconnel vessel with 20 mL of deionized water. No extra base or mineralizer was used, maintaining the close to neutral pH to minimize corrosion of the internal vessel walls. The controlled temperature of the heating block was varied between 550−700 °C, approached at a rate of 20 °C/min, producing temperatures within the vessels of 370−395 °C and pressures of 200−220 bar. Solutions that were held at these conditions for 48 h produced highly crystalline bright green rare-earth orthochromite perovskite powders. Powders were collected using suction filtration and washed with deionized water before being dried at 75 °C in air for characterization.

For transmission electron microscopy (TEM), samples were dispersed onto lacy carbon film reinforced on a copper grid from a suspension produced ultrasonically in methanol. Images and energy dispersive X-ray (EDX) spectra were recorded using a JEOL 2100 LaB$_6$ instrument operating at 200 kV. Atomic resolution High Angle Annular Dark Field Scanning Transmission Electron Microscopy (HAADF-STEM) images were recorded using an aberration corrected JEOL ARM200F operating at 200 kV. High-resolution powder X-ray diffraction (PXRD) data were collected using a Panalytical X'Pert Pro MPD equipped with monochromatic Cu K$_{\alpha 1}$ radiation and a PIXcel detector. Rietveld refinements were performed against the data using the program TOPAS-Academic implemented with jEdit (Versions 4.1 and 4.3.1 respectively).[33] Low-temperature Raman spectra were collected using a Renishaw inVia Raman Microscope with spectral cutoff at ∼120 cm^{-1} equipped with a He−Ne laser of excitation wavelength 632.8 nm. Powders were placed in a Linkam THMS 600 sample stage and cooled to 123 K under liquid nitrogen. The Raman experiments were carried out using a laser power of <1 mW focused into a ∼1 μm^2 spot to avoid local heating of the polycrystalline samples by the laser.

Shell model calculations were performed using the program GULP,[34] where the La, Sm, and Cr ions are represented by point charges, and oxygen ions are represented by a charged core and a charged massless shell linked by a spring constant k. The calculations take into account the Coulomb interaction and a short-range repulsive potential energy modeled by a Buckingham interatomic potential. The simulations of the $La_xSm_{1-x}CrO_3$ solid solutions follow a virtual ion approach and assume a random distribution of the A cations.

Magnetization data were collected using a Quantum Design Magnetic Property Measurement System (MPMS) SQUID magnetometer over the temperature range of 2−400 K. Data were collected from zero field-cooled warming (ZFCW) and field-cooled cooling (FCC) measurements made over this temperature range in an applied magnetic field of 100 Oe.

■ RESULTS AND DISCUSSION

1. TEM Observations. TEM shows the homogeneous formation of >1 μm crystals with dendritic-type morphologies for all the mixed rare-earth orthochromite perovskites, as shown for La$_{0.5}$Sm$_{0.5}$CrO$_3$ in the diffraction contrast TEM bright field image in Figure 1 (See Supporting Information for images of the entire series). Under identical conditions, crystallites of LaCrO$_3$ and SmCrO$_3$ were shown to form agglomerated particles, with the dendritic morphology that was seen previously but only as a result of the addition of surfactants or additives, such as sodium dodecyl sulfate (SDS), to the hydrothermal reaction medium.[24] It is clear that the addition of a second rare-earth ion on the A-site of the perovskite structure influences the crystal morphology, a phenomenon observed also in the high temperature hydrothermal synthesis of Ca-doped LaCrO$_3$.[35]

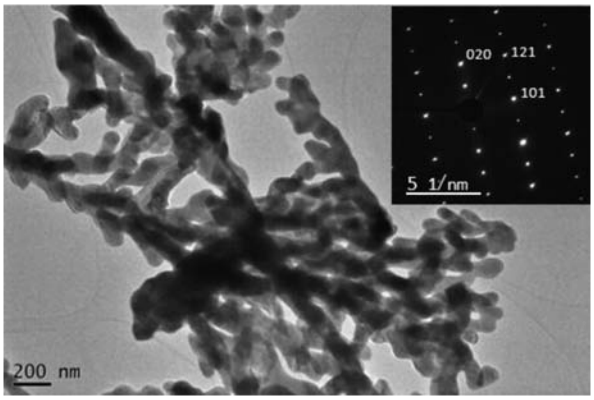

Figure 1. TEM image of hydrothermally synthesized mixed rare-earth orthochromite perovskite La$_{0.5}$Sm$_{0.5}$CrO$_3$. The inset shows an indexed selected area electron diffraction (SAED) pattern.

HAADF-STEM images show the high degree of crystallinity of the La$_{0.5}$Sm$_{0.5}$CrO$_3$ material, shown in Figure 2. This figure represents a crystallite aligned along the [101] zone axis, displaying projections of rare-earth and chromium atomic columns. The high quality of the micrographs allows for the distinction between the heavier rare-earth which appear as

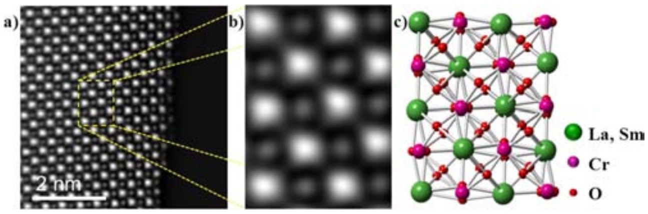

Figure 2. HAADF-STEM image of (a) $La_{0.5}Sm_{0.5}CrO_3$ crystallite aligned along the [101] zone axis, clearly displaying atomic columns of R^{3+} (brighter intensities) and Cr^{3+} (less intense) ions. (b) Shows an enlarged region which highlights the observed oxygen contrast between R^{3+} atomic columns, and (c) comparison with the crystal structure.

bigger and brighter intensities to those of the lighter chromium species that have smaller and less intense contrasts. The smearing of the signal observed between the rare-earth columns corresponds to the electron density from the oxygen as seen from comparison with the crystal structure, shown in Figure 2b. The similar atomic numbers of Sm (57) and La (62) make distinguishing between the two rare-earth species rather difficult because of their almost identical HAADF signal intensity.

2. PXRD and Structural Refinement. Figure 3 shows the Rietveld refinement of PXRD data of $La_{0.5}Sm_{0.5}CrO_3$ showing the material to be pure and well crystalline as a result of hydrothermal treatment of the precipitated amorphous hydroxide precursor at 370 °C for 48 h. It is also possible to synthesize the series of rare-earth orthochromite perovskite solid solutions $La_xSm_{1-x}CrO_3$ under these conditions in reaction durations of just 6 h. Reactions performed at temperatures lower than 370 °C yielded poorly crystalline powders containing $La(OH)_3$ impurities, while reactions performed at 240 °C for 5 days yielded mostly amorphous material that contained small amounts of crystalline $LaCO_3OH$ (see Supporting Information).

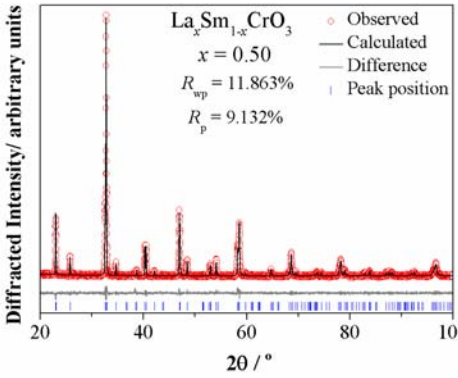

Figure 3. Rietveld refinement against high-resolution PXRD patterns of the hydrothermally synthesized mixed rare-earth orthochromite $La_xSm_{1-x}CrO_3$ solid solution $x = 0.5$. Observed (red circles), calculated (black line), difference (gray line), and peak position (blue tick marks) data calculated from the refinement are shown.

Full Rietveld refinements for all the solid solutions in the series $La_xSm_{1-x}CrO_3$ against high-resolution PXRD data show that they crystallize with a distorted perovskite structure described by orthorhombic space group *Pnma* (no. 62). The lattice parameters for the end members agree well with those in the literature for samples that have been made through both solid state and hydrothermal synthesis.[15,24] The unit cell length *a* increases slightly while both *b* and *c* decrease with increasing Sm^{3+} substitution, as seen in Table 1. The variations in the primitive unit cell lengths (a_p) and primitive unit cell volume (V_p) are shown in Figure 4. The unit cell volume decreases monotonically with increasing samarium content and is attributed to the effective ionic radius of Sm^{3+} being smaller than that of La^{3+}, at 1.079 Å and 1.160 Å, respectively (reported eight-coordinate values[36]). This is due to an increase in the distortion of the perovskite structure observed through decreasing Cr–O–Cr bond angles, which become less linear toward $SmCrO_3$. The Goldschmidt tolerance factor gives an indication of the expected distortion in ABO_3 structures and decreases from 0.898 for $LaCrO_3$ to 0.870 for $SmCrO_3$, consistent with the greater distortion as a result of increasing Sm^{3+} content.

Along with bond angles, the Cr–O bond lengths also vary with Sm^{3+} content, as shown in Figure 4d. The Cr–O1 bond lies along the *b* direction of the unit cell, and both Cr–O2(1) and Cr–O2(2) bonds are oriented in the *ac* plane. Increasing La^{3+} content results in decreasing Cr–O1 and Cr–O2(1) and increasing Cr–O2(2) bond lengths, with the average Cr–O bond length decreasing, Table 1. This, anticipated as La^{3+} is a larger ion than Sm^{3+}, causes the overall decrease in Cr–O distances, and is noted among other mixed rare-earth orthochromite perovskites,[29,32] while the values for end members $LaCrO_3$ and $SmCrO_3$ agree well with those reported previously.[16,37] The local structural distortions that are intrinsic to orthorhombic perovskites are shown as the bond length splitting increases toward the maximum, determined for $RCrO_3$

Table 1. Lattice Parameters, Cr–O Bond Lengths, Cr–O–Cr Bond and Octahedral Tilt Angles Obtained from Rietveld Refinement against PXRD Patterns for the Hydrothermally Synthesized Mixed Rare-Earth Orthochromite Perovskites[a]

$La_xSm_{1-x}CrO_3$ x	a / Å	b / Å	c / Å	V / Å^3	Cr–O1/ Å	Cr–O2(1) / Å	Cr–O2(3) / Å	Cr–O–Cr bond angle/ deg	$\varphi_{[010]}$/ deg	$\theta_{[101]}$/ deg
1.0	5.48848(4)	7.77796(6)	5.51879(4)	235.3223(29)	1.9597(62)	1.856(33)	2.055(33)	161.10(12)	5.18	9.38
0.875	5.48231(17)	7.75614(24)	5.50088(16)	233.9291(144)	1.9626(48)	1.902(19)	2.052(18)	160.30(14)	7.41	9.90
0.75	5.48687(22)	7.74497(22)	5.48311(23)	233.0085(150)	1.9667(88)	1.902(23)	2.050(23)	158.70(20)	8.12	10.76
0.625	5.48598(14)	7.72994(22)	5.46514(18)	231.7566(115)	1.9720(79)	1.921(22)	2.042(22)	157.10(16)	9.01	11.72
0.50	5.49294(11)	7.71860(17)	5.44731(12)	230.9543(85)	1.9697(44)	1.927(15)	2.031(15)	155.86(89)	8.80	12.46
0.25	5.49810(19)	7.68309(27)	5.40771(18)	228.4348(137)	1.9868(51)	1.947(17)	2.024(17)	154.00(100)	9.60	13.44
0.0	5.50385(6)	7.64364(8)	5.36567(5)	225.7308(39)	1.9899(40)	1.969(16)	1.992(15)	151.95(79)	9.99	15.82

[a] All refinements were performed using orthorhombic space group *Pnma* (no. 62). Bond lengths Cr–O2(1) and Cr–O2(3) lie in the *ac* plane, while Cr–O1 is oriented along the *b* direction. The octahedral tilt angles θ and φ describe rotations around the [101] and [010] axes, respectively, and were calculated using the equations $\theta = \arctan[4({u_{O1}}^2+{w_{O1}}^2)^{1/2}/b]$ and $\varphi = \arctan[4({u_{O2}}^2+{w_{O2}}^2)^{1/2}/(c^2+a^2)^{1/2}]$ as formulated previously.[41,52].

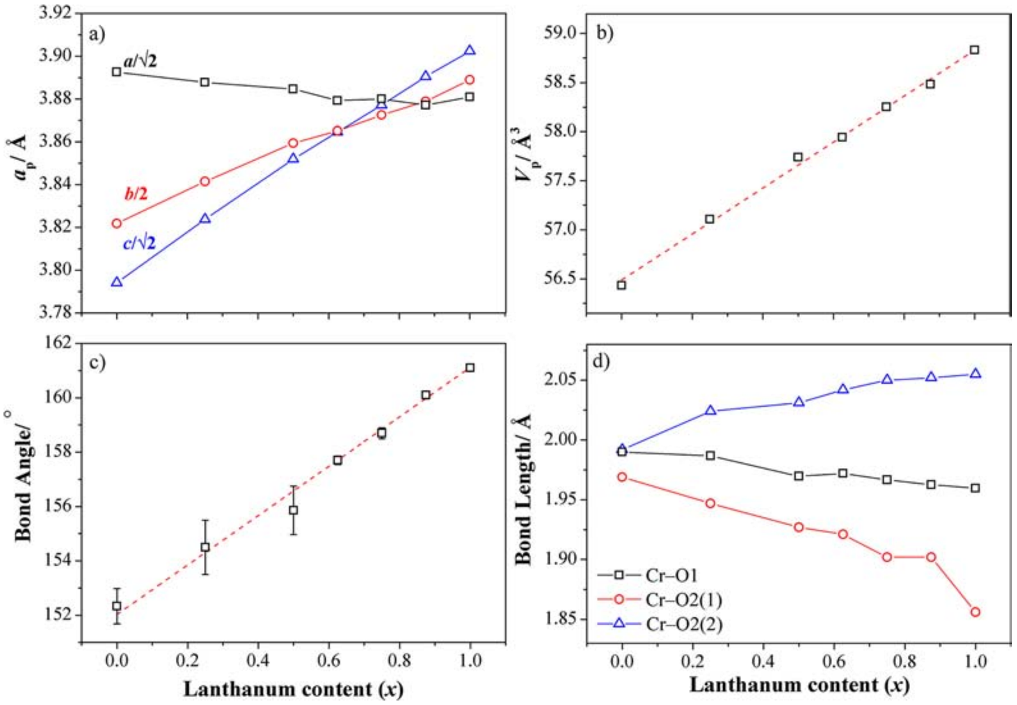

Figure 4. Variation of primitive unit cell (a) parameters (a_p), (b) volume (V_p), (c) Cr−O−Cr bond angle, and (d) Cr−O bond lengths against lanthanum content, determined from Rietveld refinement against PXRD data for the hydrothermally synthesized mixed rare-earth orthochromite perovskites $La_xSm_{1-x}CrO_3$. The dashed lines in (b) and (c) are linear fits to the data. The Cr−O1 bond is oriented along the *b* direction, while both Cr−O2(1) and Cr−O2(2) lie in the *ac* plane.

by Zhou et al.,[38] which corresponds to a rare-earth ionic radius of 1.11 Å.

3. Raman Spectroscopy. In Raman scattering the frequencies of specific lattice vibrational modes are directly related to structural distortion. The orthorhombic space group *Pnma* ($a^-b^+a^-$ tilt system[39]), distorted from ideal cubic perovskite in which Raman scattering is formally forbidden, is predicted by group theory to have 24 Raman-active modes: $\Gamma = 7\ A_g + 5\ B_{1g} + 7\ B_{2g} + 5\ B_{3g}$.[40] The number observed for the mixed rare-earth orthochromites, however, is at most 14, as shown in Figure 5; the others being either too weak in intensity or have energies below the experimental cutoff.

The low-temperature Raman spectra, with reduced thermal broadening and thus sharper bands, confirm the synthesis of genuine solid solutions of $La_xSm_{1-x}CrO_3$ and not merely mixtures of $LaCrO_3$ and $SmCrO_3$. The comparison of the solid solution spectra with those of end members $LaCrO_3$ and $SmCrO_3$ demonstrates that a mixture of the end members can be excluded. This is also supported by the observation of much broader modes for the solid solutions than end members. Owing to the increased static chemical disorder, we observe a maximum in the phonon line-width in $La_{0.5}Sm_{0.5}CrO_3$ (see Supporting Information).

The observed phonon modes are assigned to specific vibration symmetries by using data from a previous systematic Raman study that included both $LaCrO_3$ and $SmCrO_3$.[41] Figure 6 presents the Raman mode positions for the different assigned bands as a function of lanthanum content. For consistency, modes of the same symmetry are numbered according to the Raman spectrum of $SmCrO_3$, consistent with ref 41, independent of the evolution of the frequencies. From Figure 6a it can be seen that most Raman modes show a modest linear decrease in wavenumber toward $LaCrO_3$ that can be related to the increasing unit cell volume driven by the increasing average ionic radius as La^{3+} content increases. The frequency increase of the $A_g(2)$ band is understood when considering the approximation of a harmonic oscillator $\omega = (k/\mu)^{1/2}$ (*k*, force constant; μ, reduced mass). This increase shows that it is largely dominated by vibrations of the *A* cation,[41] and is thus expected to be only slightly affected by changes in the orthorhombic distortion, but rather more by the decreasing average mass with increasing La^{3+} content ($m_{Sm} = 150.36$, $m_{La} = 138.91$).

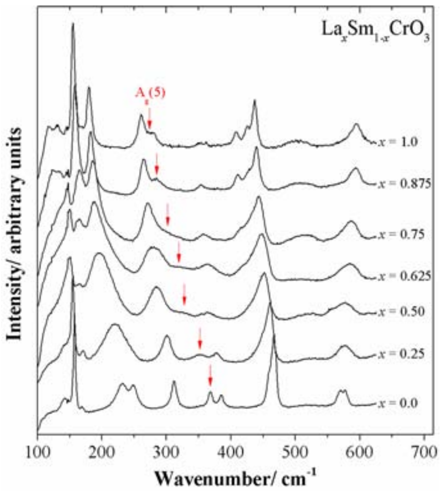

Figure 5. Raman spectra recorded at 123 K of the hydrothermally synthesized mixed rare-earth orthochromite perovskite powders, using a 632.8 nm He−Ne laser line. Arrows show how specific modes, $A_g(5)$ in this case, can be traced throughout the series.

It is shown in both Figures 5 and 6 that the low-frequency region is particularly rich, and it has already been highlighted in

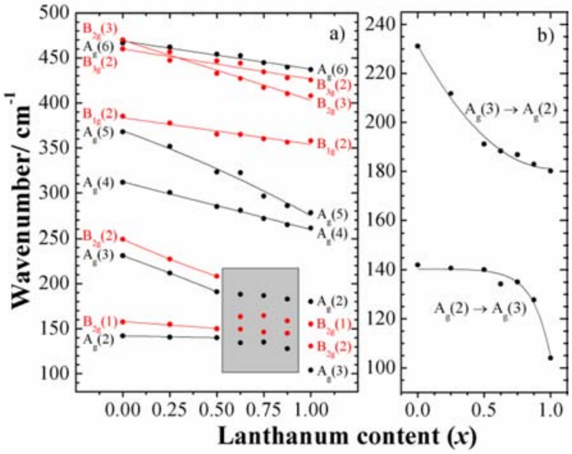

Figure 6. Raman phonon wavenumber shifts for hydrothermally synthesized mixed rare-earth orthochromite perovskites $La_xSm_{1-x}CrO_3$ as a function of lanthanum content. Lines act as guides to the eye. The gray box in (a) highlights the region of complex mode mixing referred to as the "low wavenumber region" in the text. (b) Illustrates the repulsion that is experienced by the $A_g(2)$ and $A_g(3)$ modes in this region leading to a transfer of vibrational character and intensity as indicated by the labels and as discussed in the text.

previous work that this region is characterized by a complex interaction between two A_g modes and also between two B_{2g} modes.[41] This interaction is essentially because vibrational modes of the same symmetry are not allowed to cross, but instead are expected to interact and show a so-called "mode mixing" with a transfer of their intensity and exchange of vibrational character.[42] Previous work on this region in chromites was based on the end-members $LaCrO_3$ and $SmCrO_3$ only, with the present investigation of the $La_xSm_{1-x}CrO_3$ solid solutions providing a closer observation and understanding of the mode mixing.

By extending earlier literature work,[41] we first note that the $A_g(2)$ and $A_g(3)$ modes approach each other with increasing La^{3+} content leading to a mode repulsion which is accompanied by a progressive exchange of their intensity distribution, highlighted in Figure 6b. Similarly, the drastic changes in intensity of the two modes of B_{2g} symmetry also provide evidence of mode mixing: the $B_{2g}(2)$ mode is weak in $LaCrO_3$ and yet reasonably intense in $SmCrO_3$, while the $B_{2g}(1)$ mode is very intense in $LaCrO_3$ then becomes weaker throughout the series before sharpening again in $SmCrO_3$. Although such an intensity exchange is an indication of mode mixing, its ultimate proof is the mixing of the vibrational pattern which unfortunately cannot be derived by only inspecting the experimental data. As a consequence, we have performed shell-model calculations based on the model developed for $LaCrO_3$ by Iliev et al.[43] Starting from those reported, the parameters of the Buckingham potentials were fitted to the structural data (lattice parameters and atomic positions) of the $La_xSm_{1-x}CrO_3$ solid solutions. The calculated structure was found to agree very well with the experimental data (all lattice parameters within less than 1%), with the final parameters of the model summarized in Table 2. Phonon frequencies were calculated from these parameters and are within the common accuracy of 10%. To visualize mode mixing phenomena, eigenvectors and the contribution of the atoms to each vibration mode were calculated, the evolution of which are shown in Figure 7, specifically for the A_g and B_{2g} modes of interest in the low wavenumber region. A crossover is clearly observed between a $B_{2g}(2)$ vibration mode involving only oxygen ions (i.e., octahedra) and a $B_{2g}(1)$ mode involving mainly vibrations of the *A* cations. A qualitatively similar behavior, although less pronounced, is evidenced for the A_g modes. In contrast, the atomic contributions for most other modes remain unchanged with increasing La^{3+} content, as exemplified for the low-frequency $A_g(1)$ and $B_{2g}(4)$ modes.

Table 2. Parameters of the Shell Model Used for Lattice Dynamical Calculations[a]

ion	Z/ |e|	Y / |e|	k /eV Å^{-2}	ion pair	A/eV	ρ/Å	C /eV Å^6
La	2.85			La−O	1284.6	0.3628	
Sm	2.85			Sm−O	1331.3	0.3488	
Cr	2.85			Cr−O	1717.1	0.2947	
O	0.80	−2.7	74.92	O−O	22764.0	0.1490	20.37

[a] *Z* and *Y* are the core and shell charges of an ion, respectively. The spring constant *k* links the core and the shell of the oxygen ion. The short-range Buckingham potential is defined for an ion pair as $A \exp(-r/\rho) - C/r^6$, with a cut-off radius of 12 Å.

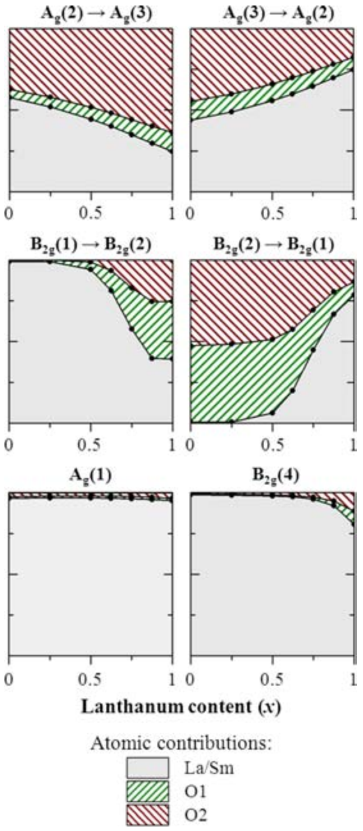

Figure 7. Atomic contributions for selected phonon modes, as calculated with the shell model, showing the mixing between $A_g(2)$ and $A_g(3)$ (respectively $B_{2g}(1)$ and $B_{2g}(2)$) modes. The atomic contributions for the $A_g(1)$ and $B_{2g}(4)$ modes, which remain almost identically dominated by A-cation motion for all compositions, are given for comparison.

We finally note that octahedral soft modes show a greater dependence than others on octahedral tilt angles and usually scale with the octahedra tilt angle.[42,44] Two such octahedral soft tilt modes are the $A_g(3)$ and $A_g(5)$ mode, previously associated with out-of-phase rotations of the CrO_6 octahedra in the [010] and [101] plane, respectively.[41] Even though these modes

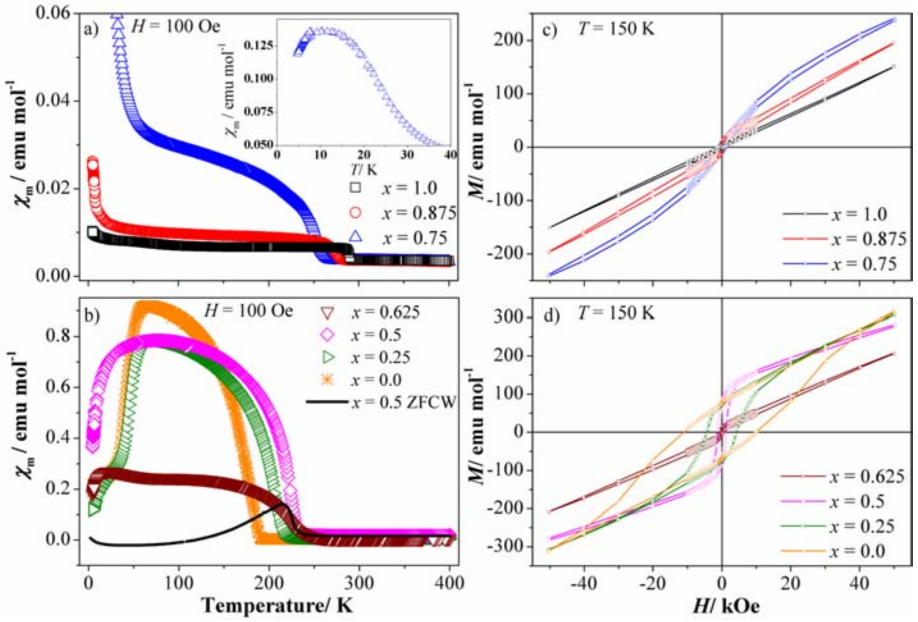

Figure 8. Temperature dependence of the molar magnetic susceptibility (χ_m) measured in an applied field of 100 Oe of the hydrothermally synthesized mixed rare-earth orthochromite perovskites $La_xSm_{1-x}CrO_3$. (a) Field-cooled cooling (FCC) data for solid solutions of $x = 1.0$ to 0.75. The inset shows the low-temperature downturn in the data at ~11 K for $La_{0.75}Sm_{0.25}CrO_3$, described in text. (b) FCC data for the further solid solutions, $x = 0.625$ to 0.0. The solid black line is the zero field-cooled warming (ZFCW) curve of $La_{0.5}Sm_{0.5}CrO_3$ showing a negative magnetization below T_N (likely because of a small negative trapped field when the sample was cooled, as described in the text) and highlighting the observed difference between FCC and ZFCW data. (c and d) Magnetization data recorded at 150 K as a function of applied field up to 50 kOe for all solid solutions.

could be in principle used to estimate the octahedra tilt angle, it is important to realize that the significant strong mode coupling inhibits such an analysis in the case of $La_xSm_{1-x}CrO_3$.

4. Magnetic Properties. It has been previously shown that the Cr^{3+} moments in all rare-earth orthochromite perovskites order with a G-type antiferromagnetic structure at their Néel temperatures,[45] which can also lead to weak ferromagnetic behavior because of a slight canting of the moments away from the antiferromagnetic axis.[24,46] The dependence of the molar magnetic susceptibilities, χ_m, with temperature for the series of hydrothermally synthesized materials are shown in Figure 8a and b. The data were recorded in an applied field of 100 Oe and have been grouped together according to their magnitude below the ordering temperatures to allow for direct comparison. Only Cr^{3+} carries a magnetic moment (spin-only $S = 3/2$) in $LaCrO_3$, but for solid solutions ($0.0 \leq x \leq 0.875$) there is also a moment present on the rare-earth site carried by Sm^{3+} ($S = 5/2$). The increasing magnitude of the magnetic susceptibility observed below the ordering temperature for each material as the level of magnetic samarium increases is explained by coupling between Cr^{3+} and Sm^{3+} spins. Below T_N the ordered moments of the Cr^{3+} sublattice polarize those of the Sm^{3+},[47] causing an enhancement of the magnetization observed as a result of Sm^{3+} doping. In solid solutions with high x, the small amount of Sm^{3+} acts as a paramagnetic impurity and therefore dominates the magnetization at low temperature. It is only when sufficient isotropic distribution of Sm^{3+} ions is achieved that the magnetization is enhanced immediately below T_N because of polarization. This enhancement is also evident from the magnetization data recorded at 150 K (below T_N) as a function of applied field, where hysteric behavior increases with Sm^{3+} content (Figure 8c and d). The remanent magnetization and coercive field reach their maxima in solid solutions of x = 0.5 and x = 0.0 respectively, with saturation of the slight ferromagnetic component occurring at fields above 40 kOe, as seen in Figure 8 d.

At low temperatures a second transition is observed in the magnetic susceptibility data of all orthochromites except $LaCrO_3$, and this is attributed to the second-order spin reorientation of the Cr^{3+} moments from $\Gamma_4(G_x, A_y, F_z)$ to the $\Gamma_2(F_x, C_y, G_z)$ configuration. It should be noted that these configurations and the description of the reorientation below are written with the crystallographic axes in the *Pbnm* setting. Above this temperature T_{SR} the antiferromagnetic Cr^{3+} axis is aligned along the *a* crystallographic axis and is shown to undergo a continuous rotation to the *c* axis on cooling through T_{SR},[48] while the weak ferromagnetic axis, caused by slight canting, rotates from the *c* to the *a* axis.[49] The antiparallel polarization of the Sm^{3+} spins to the weak ferromagnetic Cr^{3+} moment causes a rapid decrease in the magnitude of the susceptibility below T_{SR}.[47] This is clearly observed where the data downturn at low temperatures; even in the solid solution x = 0.25 where a maximum is observed at ~11 K (see Figure 8 a) inset). The data for end member $SmCrO_3$ show this spin-reorientation to occur at T_{SR} ~33 K, in good agreement with the second-order spin reorientation reported previously.[48] The temperature of this spin reorientation T_{SR} decreases with increasing x; explained by strengthening superexchange pathways as the statistical probability of neighboring Sm^{3+} ions increases. These Sm^{3+}—Cr^{3+} interactions are responsible for this behavior, so no spin-reorientation is observed for solid solutions with high x, or indeed for $LaCrO_3$ with nonmagnetic La^{3+}.[47]

Further evidence for coupling between the Cr^{3+} and the increasing number of Sm^{3+} spins is shown most clearly in the x = 0.5 solid solution, where there are dramatic differences between the ZFCW and FCC data (see Figure 8b). The FCC data show the susceptibility increases on cooling as the material orders below T_N = 240 K. However the ZFCW data suggest that there was a small negative trapped field present in the superconducting magnet of the SQUID magnetometer when the powder was cooled to 2 K, since on warming χ_m decreases through zero at 4.6 K before becoming positive again above 118 K, overlaying with the FCC data. As the material was cooled, the Cr^{3+} moments order antiferromagnetically along the negative direction of this trapped field explaining the negative curve below T_N observed on warming. At very low temperatures, the susceptibility from the Sm^{3+} moments is larger, and they are aligned antiparallel to the Cr^{3+} sublattice, generating the small positive signal observed below 4.6 K. This decreases with increasing temperature as the susceptibility becomes dominated by the Cr^{3+} signal. Similar behavior is observed in other orthochromite perovskites, $La_{0.5}Pr_{0.5}CrO_3$ and $GdCrO_3$, and has been attributed to the rare-earth sublattice being polarized antiparallel to the small ferromagnetic component originating from canted antiferromagnetically ordered Cr^{3+} moments.[50,51]

The Néel temperatures T_N, below which the Cr^{3+} moments are antiferromagnetically ordered, are given in Table 2, and those for end members $LaCrO_3$ and $SmCrO_3$ agree well with those previously reported. A monotonic decrease is observed between T_N and increasing Sm^{3+} content and therefore increasing structural distortion also, shown in Figure 9. Identical behavior has been observed through the entire series of single rare-earth orthochromites $RCrO_3$ (R = La to Lu),[24,38] and also mixed rare-earth chromites $La_{1-x}R_xCrO_3$ (where R = Pr, Nd, and Gd).[28,30,32] The superexchange interactions between adjacent Cr^{3+} ions causing this cannot be accounted for by the decreasing Cr−O−Cr bond angles alone. The change in T_N was shown to be strongly dependent on *t-e* orbital hybridization introduced from the intrinsic distortions in orthorhombic $RCrO_3$ perovskites that cause overlap of the π and σ bonds between adjacent $Cr^{3+}(t^3e^0)$ ions.[38]

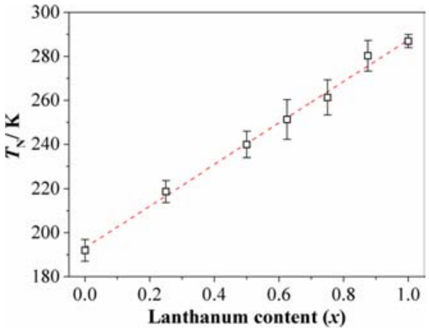

Figure 9. Variation of the antiferromagnetic Néel temperatures T_N with lanthanum content of the hydrothermally synthesized mixed rare-earth orthochromite perovskites $La_xSm_{1-x}CrO_3$. These temperatures correspond to the ordering of the Cr^{3+} moments and were determined from ZFCW and FCC data.

At high temperatures all solid solutions of $La_xSm_{1-x}CrO_3$ display Curie−Weiss behavior, and the inverse molar magnetic susceptibility χ_m^{-1} data is shown in Figure 10. With adequate temperature ranges (>100 K) between T_N and the maximum measurement temperature of 400 K, the paramagnetic regions of the data are fitted using $\chi_m(T) = C/(T - \theta) + \chi_o$, to determine the Curie constant C and Weiss temperature θ. Knowledge of such values allows for the calculation of individual effective moments μ_{eff} of the Sm^{3+} and Cr^{3+} ions, given in Table 3. The measured moment of $LaCrO_3$ indicates that Cr^{3+} is present in its high spin state (S = 3/2) with moments close to the expected value of 3.87 μ_B; if it were in the low spin state (S = 1/2) a lower value of 1.73 μ_B would be expected. As expected, the effective moment increases with decreasing x as more nonmagnetic La^{3+} is substituted for Sm^{3+}.

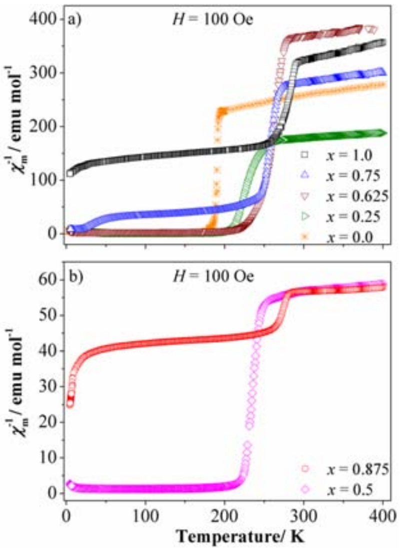

Figure 10. Temperature dependence of the inverse molar magnetic susceptibility (χ_m^{-1}) for the hydrothermally synthesized mixed rare-earth orthochromite perovskites $La_xSm_{1-x}CrO_3$. The data were collected under field-cooled cooling (FCC) conditions in an applied field of 100 Oe, and are grouped according to their magnitude.

Table 3. Magnetic Parameters of the Hydrothermally Synthesized Mixed Rare-Earth Orthochromite Perovskites

$La_xSm_{1-x}CrO_3$ x	T_N/ K^a	$\lvert\theta\rvert$/ K	C/ μ_B	μ_{eff}/ μ_B^{d}	μ_{Sm}^{3+}/ μ_B^{e}	μ_{Cr}^{3+}/ μ_B^{f}
1.0	289^b	633.8	2.985	4.887	0	4.887
0.875	279	2962.8	23.53	13.72		
0.75	261	843.1	4.085	5.717	4.208	5.713
0.625	251	1243.8	4.204	5.799	4.319	5.790
0.50	240	834.4	4.872	6.243	4.899	6.229
0.25	219	1091.2	7.299	7.641	6.588	7.615
0.0	192^c	613.4	7.432	7.711	6.669	7.665

[a] T_N corresponds to the antiferromagnetic ordering temperature of Cr^{3+} moments. The Weiss temperature (θ) and Curie constant (C) are extracted by fitting the paramagnetic region of the data. [b] Reported Néel temperatures for $LaCrO_3$ are 288,[16,50] 287,[24] 295,[45] and 282[53] K. [c] Reported Néel temperatures for $SmCrO_3$ are 197,[16] 192,[24,49] 193,[46] and 190[48] K. [d] The effective magnetic moment per formula unit μ_{eff}, calculated from $\mu_{eff}^2 = 3k_BC/N_A\mu_B^2$, is used to calculate moments on the Cr^{3+} and Sm^{3+} sites through $\mu_{eff} = [(\mu_{Sm}{}^{3+})^2 + (\mu_{Cr}{}^{3+})^2]^{1/2}$. [e] $\mu_{Sm}{}^{3+}$ is calculated assuming a full spin-only moment S = 3/2 on the B site. The theoretical moment of Sm^{3+} is calculated to be 0.84 μ_B from $g[J(J+1)]^{1/2}$, where g is the Landé g-factor, $g = 1 + [J(J+1) + S(S+1) - L(L+1)/2J(J+1)]$, with J and L being the total angular momentum and orbital angular momentum, respectively. [f] $\mu_{Cr}{}^{3+}$ is calculated assuming a full J moment on the A site, which is diluted as a function of x. The theoretical moment carried by Cr^{3+} is 3.87 μ_B, calculated from $2[S(S+1)]^{1/2}$, where S = 3/2 for the high-spin configuration.

The Weiss temperatures θ for these materials are very high compared to their antiferromagnetic Néel temperatures. We calculate θ for $LaCrO_3$ to be 633 K, slightly reduced from the reported values of 750 and 800 K.[24,46] Such discrepancies could be due to the possibility of these materials containing certain amounts of frustration, as postulated previously.[24]

■ CONCLUSIONS

A new series of materials have been successfully synthesized using a hydrothermal route, and all of the collected data confirm the formation of homogeneous solid solutions of mixed rare-earth orthochromite perovskites $La_xSm_{1-x}CrO_3$ with orthorhombic *Pnma* structure. The structural distortion quantified by lattice parameters and octahedral tilt angles depends greatly upon the A-site composition and increases toward $SmCrO_3$, as shown by PXRD and Raman scattering data. The subtle structural distortions accompanying slight changes in Sm^{3+} content have significant effect on the magnetic properties of the material. Phonon Raman mode assignments have been made for the solid solutions through analysis of the complex shifts throughout the series. Aided by shell-model calculations the mode assignment and coupling phenomena in the complicated low wavenumber region below 250 cm^{-1} have been clarified.

■ ASSOCIATED CONTENT

Ⓢ Supporting Information

Further details of synthesis (Figure S1), results from Rietveld refinement of PXRD data (Figure S2, Tables S1 and S2), Raman scattering (Figure S3, Table S3), and TEM (Figure S4). This material is available free of charge via the Internet at http://pubs.acs.org.

■ AUTHOR INFORMATION

Corresponding Author

*E-mail: r.i.walton@warwick.ac.uk.

Notes

The authors declare no competing financial interest.

■ ACKNOWLEDGMENTS

We thank the EPSRC and the STFC Centre for Materials Physics and Chemistry for cofunding this work (CMPC11104). Some of the instruments used at the University of Warwick were obtained through the Science City Advanced Materials project "Creating and Characterising Next Generation Advanced Materials" with support from Advantage West Midlands (AWM) and part funded by the European Regional Development Fund (ERDF). We thank Dr. David Walker for his assistance with measuring high-resolution powder XRD patterns.

■ REFERENCES

(1) Rao, C. N. R.; Sundaresan, A.; Saha, R. *J. Phys. Chem. Lett.* **2012**, *3*, 2237.

(2) Mitchell, R. H. *Perovskites: Modern and Ancient*; Almaz Press Inc.: Thunder Bay, ON, Canada, 2002.

(3) Attfield, J. P. *Chem. Mater.* **1998**, *10*, 3239.

(4) Siemons, M.; Simon, U. *Sens. Actuators, B* **2007**, *126*, 181.

(5) Russo, N.; Mescia, D.; Fino, D.; Saracco, G.; Specchia, V. *Ind. Eng. Chem. Res.* **2007**, *46*, 4226.

(6) Fergus, J. *Solid State Ionics* **2004**, *171*, 1.

(7) Liu, Z.; Dong, D.; Huang, X.; Lü, Z.; Sui, Y.; Wang, X.; Miao, J.; Shen, Z. X.; Su, W. *Electrochem. Solid-State Lett.* **2005**, *8*, A250.

(8) Shen, Y.; Liu, M.; He, T.; Jiang, S. P. *J. Power Sources* **2010**, *195*, 977.

(9) Beckers, J.; Rothenberg, G. *ChemPhysChem* **2005**, *6*, 223.

(10) Spaldin, N. A.; Fiebig, M. *Science* **2005**, *309*, 391.

(11) Zvezdin, A. K.; Mukhin, A. A. *JETP Lett.* **2008**, *88*, 505.

(12) Sahu, J. R.; Serrao, C. R.; Ray, N.; Waghmare, U. V.; Rao, C. N. R. *J. Mater. Chem.* **2007**, *17*, 42.

(13) Serrao, C.; Kundu, A.; Krupanidhi, S.; Waghmare, U. V.; Rao, C. *Phys. Rev. B* **2005**, *72*, 220101.

(14) Rajeswaran, B.; Khomskii, D. I.; Zvezdin, A. K.; Rao, C. N. R.; Sundaresan, A. *Phys. Rev. B* **2012**, *86*, 214409.

(15) Geller, S. *Acta Crystallogr.* **1957**, *10*, 243.

(16) Prado-Gonjal, J.; Schmidt, R.; Romero, J.-J.; Ávila, D.; Amador, U.; Morán, E. *Inorg. Chem.* **2013**, *52*, 313.

(17) Parkin, I. P.; Komarov, A. V.; Fang, Q. *Polyhedron* **1996**, *15*, 3117.

(18) Kuznetsov, M. V.; Parkin, I. P. *Polyhedron* **1998**, *17*, 4443.

(19) Inagaki, M.; Yamamoto, O.; Hirohara, M. *J. Ceram. Soc. Jpn.* **1990**, *98*, 675.

(20) Devi, P. S. *J. Mater. Chem.* **1993**, *3*, 373.

(21) Kikkawa, T.; Yoshinaka, M.; Hirota, K.; Yamaguchi, O.; Tanabe, K. *J. Mater. Sci. Lett.* **1995**, *14*, 1071.

(22) Vernoux, P.; Djurado, E.; Guillodo, M. *J. Am. Ceram. Soc.* **2001**, *95*, 2289.

(23) Modeshia, D. R.; Walton, R. I. *Chem. Soc. Rev.* **2010**, *39*, 4303.

(24) Sardar, K.; Lees, M. R.; Kashtiban, R. J.; Sloan, J.; Walton, R. I. *Chem. Mater.* **2011**, *23*, 48.

(25) Yoshimura, M.; Song, S. T.; Sōmiya, S. *Yogyo Kyokai Shi* **1982**, *90*, 91.

(26) Song, S. T.; Pan, H. Y.; Wang, Z.; Yang, B. *Ceram. Int.* **1984**, *10*, 143.

(27) Zheng, W.; Pang, W.; Meng, G.; Peng, D. *J. Mater. Chem.* **1999**, *9*, 2833.

(28) Yoshii, K.; Nakamura, A.; Ishii, Y.; Morii, Y. *J. Solid State Chem.* **2001**, *162*, 84.

(29) Taguchi, H.; Nagao, M. *J. Solid State Chem.* **1995**, *114*, 236.

(30) Sharma, N.; Srivastava, B. K.; Krishnamurthy, A.; Nigam, A. K. *Solid State Sci.* **2010**, *12*, 1464.

(31) Chakraborty, K. R.; Das, A.; Yusuf, S. M.; Krishna, P. S. R.; Tyagi, A. K. *J. Magn. Magn. Mater.* **2006**, *301*, 74.

(32) Du, Y.; Cheng, Z. X.; Wang, X.-L.; Dou, S. X. *J. Appl. Phys.* **2010**, *108*, 93914.

(33) Coelho, A. A. *J. Appl. Crystallogr.* **2000**, *33*, 899.

(34) Gale, J. D.; Rohl, A. L. *Mol. Simul.* **2003**, *29*, 291.

(35) Rivas-Vázquez, L. P.; Rendón-Angeles, J. C.; Rodríguez-Galicia, J. L.; Gutiérrez-Chavarria, C. A.; Zhu, K. J.; Yanagisawa, K. *J. Eur. Ceram. Soc.* **2006**, *26*, 81.

(36) Shannon, R. D. *Acta Crystallogr., Sect. A* **1976**, *32*, 751.

(37) Oikawa, K.; Kamiyama, T.; Hashimoto, T.; Shimojyo, Y.; Morii, Y. *J. Solid State Chem.* **2000**, *154*, 524.

(38) Zhou, J.-S.; Alonso, J. A.; Pomjakushin, V.; Goodenough, J. B.; Ren, Y.; Yan, J.-Q.; Cheng, J.-G. *Phys. Rev. B* **2010**, *81*, 214115.

(39) Glazer, A. M. *Acta Crystallogr., Sect. B* **1972**, *28*, 3384.

(40) Iliev, M. N.; Abrashev, M. V.; Lee, H.-G.; Popov, V. N.; Sun, Y. Y.; Thomsen, C.; Meng, R. L.; Chu, C. W. *Phys. Rev. B* **1998**, *57*, 2872.

(41) Weber, M.; Kreisel, J.; Thomas, P.; Newton, M.; Sardar, K.; Walton, R. *Phys. Rev. B* **2012**, *85*, 54303.

(42) Iliev, M.; Abrashev, M.; Laverdière, J.; Jandl, S.; Gospodinov, M.; Wang, Y.-Q.; Sun, Y.-Y. *Phys. Rev. B* **2006**, *73*, 3.

(43) Iliev, M.; Litvinchuk, A.; Hadjiev, V.; Wang, Y. Q.; Cmaidalka, J.; Meng, R.-L.; Sun, Y.-Y.; Kolev, N.; Abrashev, M. *Phys. Rev. B* **2006**, *74*, 214301.

(44) Scott, J. F. *Phys. Rev.* **1969**, *183*, 823.

(45) Weinberg, I.; Larsen, P. *Nature* **1961**, *192*, 445.

(46) Bertaut, E. F.; Bassi, G.; Buisson, G.; Burlet, P.; Chappert, J.; Delapalme, A.; Mareschal, J.; Roult, G.; Aleonard, R.; Pauthenet, R.; Rebouillat, J. P. *J. Appl. Phys.* **1966**, *37*, 1038.

(47) Yamaguchi, T. *J. Phys. Chem. Solids* **1974**, *35*, 479.

(48) Gorodetsky, G.; Hornreich, R. M.; Shaft, S.; Sharon, B.; Shaulov, A.; Wanklyn, B. M. *Phys. Rev. B* **1977**, *16*, 515.

(49) Tsushima, K.; Aoyagi, K.; Sugano, S. *J. Appl. Phys.* **1970**, *41*, 1238.
(50) Yoshii, K.; Nakamura, A. *J. Solid State Chem.* **2000**, *155*, 447.
(51) Cooke, A. H.; Martin, D. M.; Wells, M. R. *J. Phys. C: Solid State Phys.* **1974**, *7*, 3133.
(52) Mountstevens, E.; Redfern, S.; Attfield, J. *Phys. Rev. B* **2005**, *71*, 220102.
(53) Gordon, J. D.; Hornreich, R. M.; Shtrikman, S.; Wanklyn, B. M. *Phys. Rev. B* **1976**, *13*, 3012.